Enhanced thermal fingering in a shear-thinning fluid flow through porous media: dynamic pore network modelling

DOI:
https://doi.org/10.1063/5.0080375

Document Version
Accepted author manuscript

Enhanced thermal fingering in a shear-thinning fluid flow through porous media: dynamic pore network modelling

Senyou An,[1,2] Muhammad Sahimi,[3] Takshak Shende,[1] Masoud Babaei,[1] and Vahid Niasar*[1]

[1)]*Department of Chemical Engineering & Analytical Science, The University of Manchester, Manchester, M13 9PL, UK*

[2)]*Department of Earth Science and Engineering, Imperial College London, South Kensington Campus, London, SW7 2AZ, UK*

[3)]*Mork Family Department of Chemical Engineering and Materials Science, University of Southern California, CA, 90089-1211, USA*

(*Electronic mail: vahid.niasar@manchester.ac.uk)

(Dated: 17 January 2022)

Thermal-viscous fingering instability in porous media is a common phenomenon in nature, as well as in many scientific problems and industrial applications. Despite the importance, however, thermal transport in flow of a non-Newtonian fluid in porous media and the resulting fingering has not been studied extensively, especially if the pore space is heterogeneous. In this paper, we propose a pore network model with fully graphics processing unit (GPU)-parallelized acceleration to simulate thermal transport in flow through three-dimensional (3D) unstructured pore networks at centimeter scale, containing millions of pores. A thermal Meter equation is proposed to model temperature- and shear stress-dependent rheology of the non-Newtonian fluids. After comparing the simulation results with an analytical solution for the location of the thermal front in a spatially-uncorrelated pore network, thermal transport in flow of both Newtonian and non-Newtonian fluids is studied in the spatially uncorrelated and correlated pore networks over a range of injection flow rates. The simulations indicate that the injection flow rate, the shear-thinning rheology, and the morphological heterogeneity of the pore space all enhance thermal-viscous fingering instability in porous media, but with distinct patterns. In spatially-correlated networks, the average temperature and apparent viscosity at the breakthrough point in flow of a shear-thinning fluid exhibit non-monotonic dependence on the injection flow rate. Analysis of the fractal dimension of thermal patterns at the breakthrough point supports the conclusion. The results highlight the importance of designing optimal flow conditions for application purposes.

I. INTRODUCTION

Heat transfer in porous media is a common phenomenon in nature, as well as in many scientific and industrial problems, ranging from heat transfer in magma in Earth's crust[1] and in cementing and drilling fluids[2], to thermal recovery of heavy oil[3], thermal insulation systems[4], ceramic processing[5], filtration processes[6], heat flow in a proton exchange membrane fuel cells[7], and drying of porous media[8]. Although in the studies of heat transfer in flow systems it is often assumed that the fluids are Newtonian, no real fluid fits perfectly the definition of Newtonian rheology, even though some fluids, such as water and air, can be approximated by the Newtonian rheology. Recent molecular simulation for the flow of water in small pores and tubes indicated that, under a variety of conditions, water follows non-Newtonian, and in particular shear-thinning rheology[9] in which case its viscosity is dependent upon the hydrodynamics of the system, such as the shear rate, in addition to the fact that it is also a function of the temperature regardless of its rheological equation of state.

In order to upscale heat and mass transfer in flow of non-Newtonian fluids in porous materials, one must deal with a system whose complexity is fourfold: (a) spatial (and temporal) variability of the shear rate, viscosity, and shear stress in the pore space; (b) preferential flow pathways of the fluids due to the spatial-statistical distribution of pore and throat sizes; (c) energy transfer across solid-fluid interfaces; and (d) chemical and mineralogical heterogeneity across distinct length scales. In the present paper, we address how the morphological heterogeneity of a porous medium affects heat and mass transfer in flow of a non-Newtonian fluid in a porous medium, demonstrating that it leads to instabilities in heat transfer, which we refer to as thermal fingering.

To study thermal transport in flow of a Newtonian fluid through porous media, many experimental, analytical, and numerical approaches have been proposed. For example, based on the particle image velocimetry (PIV) and liquid crystal thermography (LCT) measurements, the pore-scale velocity and temperature distribution were generated and visualized in a refractive index-matched porous medium[10]. Accurate recording of the dynamic evolution of the temperature in 3D porous media, particularly at pore-scale, is still an unsolved problem. To estimate the upscaled thermal parameters, such as thermal conductivity, and the convective heat transfer coefficient, several analytical approaches have been proposed for simple systems[11,12]. In addition, various theoretical approaches for thermal transport in a certain class of porous media, such as packing of overlapping or non-overlapping particles, have been suggested and analyzed, comprehensive

reviews of which are given by Torquato and Haslach Jr[13]. Moreover, in systems with regular and well-defined geometry, such as circular pipes and annular flow between concentric pipes with or without homogeneous porous media inside and known boundary conditions, the steady-state temperature distribution can be derived using such techniques as the volume-averaging method, and assuming that the flow is in the Darcy, Brinkman, or Forchheimer models[14–16]. Such models and approaches represent oversimplifications that restrict their utility, as the dynamic thermal pattern in a heterogeneous porous medium cannot be analytically predicted, but do provide useful checks for numerical simulations in simplified geometries. To study the dynamics of pore-scale thermal transport, several numerical approaches, such as direct numerical simulation[17–19] and pore-network models (PNMs) have been developed (see below).

Compared with the direct numerical simulations in images of porous media, the PNMs have a lower computational cost and higher numerical stability. They require, however, geometrical simplifications, as the PNMs are not exact representations of the pore-scale morphology of porous media. Despite this, the PNMs have been highly successful in studies of various phenomena in porous media, and have been widely leveraged in recent years for simulating thermal transport in porous media, especially as a tool to study phase-change of water as a Newtonian fluid[7,20–22]. Most of such research was realized using the PNMs with regular connectivity, such as a simple-cubic network, in order to simplify the calculation of local thermal equilibrium. In 3D regular pore networks, Surasani, Metzger, and Tsotsas[23,24] studied drying of porous media by proposing a non-isothermal PNM. With the consideration of heat exchange between the fluid and solid,Belgacem, Prat, and Pauchet[25] proposed a structured and collocated solid and fluid network to simulate the formation of liquid water in the proton-exchange membrane fuel cell. Koch *et al.*[26] proposed an unstructured dual network, consisting of pores and grains, to simulate the coupled liquid water flow and heat transfer in both the void space and the solid matrix. Due to the high computational cost of such algorithms, the domain in such simulation is, however, usually small with only hundreds to thousands of pores, because dynamic updating of the pressure, velocity, and temperature, plus phase change that may occur at each time step require considerable calculations. Thus, the size of the simulation domain limits the scope of a study of the effect of heterogeneity in porous media on such phenomena. Recently, however, An *et al.*[27] developed a fully graphical processing unit (GPU)-based algorithm for PNM simulations in order to accelerate the associated computations. In particular, the velocity field is computed in a matter of several seconds in a network with millions of pores.

On the other hand, thermal transport in flow of a non-Newtonian fluid in porous media, though highly important for many natural and industrial applications, has not received the attention that it deserves. The viscosity of a non-Newtonian fluid is a function of the shear rate and is usually sensitive to temperature variations[28,29]. Several empirical models for non-Newtonian rheology have been proposed for predicting the relation between the viscosity and shear rate, such as the Cross[30], Carreau-Yasuda[31], and Meter[32] models for power-law fluids. Sorbie, Clifford, and Jones [33] developed a 2D PNM to investigate the rheology of pseudoplastic fluids in porous media. For power-law fluids in a square grid network, Pearson and Tardy [34] and Perrin *et al.* [35] studied the flow of a non-Newtonian fluid and the effect of tortuosity on the transport process. Using networks extracted from actual porous media, Lopez, Valvatne, and Blunt [36] studied the flow of shear-thinning fluid and compared the results with four experiments. Following a similar approach, the flow of a non-Newtonian fluid in pore networks without the thermal effect was studied[37–40]. It should, however, be pointed out that all such studies were under isothermal conditions.

Since the properties of fluids vary with temperatures, the same fluid at different temperatures may be assumed as being distinct. In this way, the instability of the front, usually referred to as the Saffman–Taylor instability for miscible fluids, was studied[41,42]. Kong, Haghighi, and Yortsos [43] were presumably the first to report pore-scale experimental visualization of thermal transport by analyzing the steam flooding of heavy oil in a Hele-Shaw cell, i.e., the channel between two flat surfaces with a small gap between them. Following their work, others carried out experimental studies of displacement by steam in 2D micromodels[44–48]. Kuang, Maxworthy, and Petitjeans [49] conducted experiments in a transparent capillary tube, studying the displacement of a high-viscosity fluid at low temperature by the same fluid but at a higher temperature with lower viscosity, and analyzed the instability and Saffman-Taylor fingering. Thermal-viscous instability in a Hele-Shaw cell was widely analyzed by experiments[50,51]. In addition, some numerical simulation methods were proposed to investigate thermal-viscous fingering instability in a porous medium at the continuum scale or/and in simple models[52–54].

The present study aims at making two new contributions. One is upscaling thermal and hydrodynamic properties of shear-thinning fluids under non-isothermal conditions, which demonstrates how the instability in thermal transport leads to nonlinearity in the upscaled flow properties. To our knowledge, there is no pore-scale simulation study that incorporates non-Newtonian fluid flow under non-isothermal conditions in porous media, which is the second contribution of the present work. In addition to the focus of the work on non-isothermal transport in flow of a non-Newtonian

fluid, our work features the use of a GPU-accelerated algorithm for simulating fluid flow and heat transport in 3D unstructured networks, a unique feature that allows large pore-scale simulations in correlated and uncorrelated pore networks with about one million pore bodies (see Section II B).

The rest of this paper is organized as follows. First, we introduce theoretical background for the governing equations of mass, momentum, and energy transport in porous media, a rheological model for the non-Newtonian fluid, and a numerical scheme used in the simulations (Section II C and II D). Then, we describe how the correlation length of the spatial heterogeneity in the pore network affects thermal instability in flow of non-Newtonian fluids in porous materials (Section III). The last section summarizes the paper and presents the main conclusions. In the Appendices, we present a comparison between of thermal fronts determined by simulations and the analytical solutions, the difference between thermal fingering in 3D structured and unstructured networks, the effect of a solid phase on heat transfer, the distribution of shear stress and viscosity at pore scale, and the impact of a shear-thickening fluid on thermal fingering patterns.

II. METHODOLOGY

We first describe the problem that we study, the model that we have developed, and the rheology of the non-Newtonian fluid.

A. Problem definition and assumptions

We study flow and heat transfer in a heterogeneous porous medium, fully saturated by a shear-thinning fluid. Thus, we first provide a brief description of the model, and the assumptions that have been made.

- The porous medium is represented by a network of spherical pore bodies connected by cylindrical pore throats. A disk-shape geometry in which the thickness is much smaller than the radial extension of the disk is used. The fluid is injected at the central point of the disk. The motivation for using the disk-shaped geometry is that many experimental studies of displacement of instability were carried out in porous media with such a geometry. Thus, we hope that our work with non-isothermal flow of non-Newtonian fluid will motivate similar experimental studies, so that the data could be compared with our results.

- Slow fluid flow is assumed, so that Hagen-Poiseuille equation can be used.

- Initially, the pore network is fully saturated by either a shear-thinning fluid or by a Newtonian fluid.

- The dynamic viscosity of the fluid depends on both temperature and the shear rate, while the fluid's density is temperature-dependent.

- Heat transfer in both the solid matrix and the pore space is explicitly taken into account.

- It is assumed that no phase change occurs in the temperature range that we study.

- Viscous dissipation and radiation are neglected.

B. Generation of pore network

For better visualization, the 3D disk-shaped pore networks with a radius of 5.0 cm and a height of 0.1 mm were generated. The networks contain about one million pore bodies and four million pore throats that, to our knowledge, constitute some of the largest PNMs ever used in such studies. To study the effect of the spatial correlations in the pore sizes, both uncorrelated and correlated networks were generated, as shown in Fig. 1. By "homogeneous" we mean that the pores are spatially uncorrelated. That means networks larger than the representative elementary volume (REV), networks are *macroscopically homogeneous*. The correlated network had a correlation length of 0.25 cm. As shown by An *et al.* [27], the maximum correlation length should be about 1/20 of the domain size to guarantee the results are independent of the generated realization.

The network generation was done by the following steps: (a) assigning pore bodies' locations, by randomly generating them using an on-chip entropy source[55]; (b) generating the network by assigning pore throats, using the Delaunay triangulation method. To reflect the statistical information of natural porous materials, the average coordination number - number of pore throats connected to the same pore body - was controlled by eliminating some of pore throats; (c) generating a continuous correlated field using a log-normal distribution field with specific correlation length; and (d) assigning the sizes of pore bodies and throats by mapping the continuous field onto the pore network.

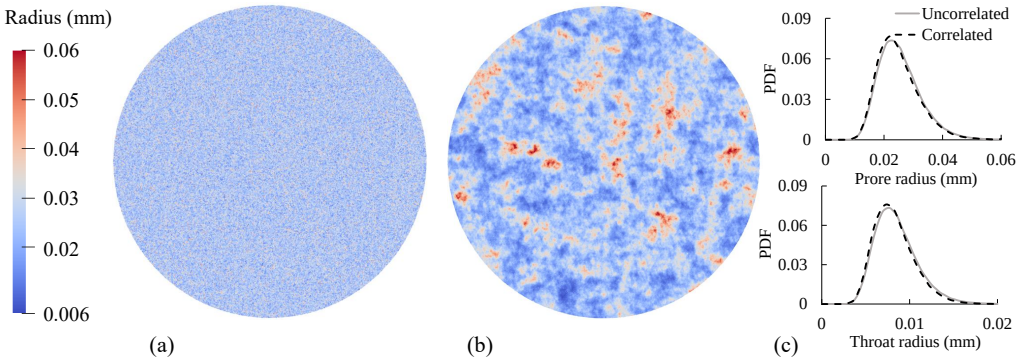

FIG. 1. The pore-size distribution of (a) spatially uncorrelated and (b) correlated pore networks with (c) the same statistics and similar pore-size distributions. In the correlated network, the correlation length is 1/20 of the network size.

C. Pore network modelling

Fluid flow in the pore network was simulated by writing down the mass balance with given boundary conditions, imposed on the network, for each pore unit, defined as the assembly of a pore body and half-length of pore throats connected to it.

The residual Res_i for the mass balance for pore unit i is given by[56], with Res_i being zero when the mass balance is satisfied.

$$\mathrm{Res}_i = \sum_{j=1}^{n} \rho_{ij} k_{ij} \left[\Delta P_{ij} + 0.5 \left(\rho_i + \rho_j \right) g \left(z_j - z_i \right) \right] = 0, \tag{1}$$

where n is the coordination number of pore body i, k_{ij} represents the flow conductance of throat ij, ΔP_{ij} is the pressure difference between pore bodies i and j, g denotes the gravity acceleration, z_i is the absolute height of pore body i, ρ_i is the fluid density in pore i, and ρ_{ij} is the density of fluid in the pore throat, $\rho_{ij} = 0.5(\rho_i + \rho_j)$. The density and temperature of the fluid were assumed uniform in each pore.

Cylindrical shapes were assigned to pore throats. Thus, the hydraulic conductance k_{ij} were calculated using the Hagen-Poiseuille equation:

$$k_{ij} = \frac{\pi r_{ij}^4}{8 \eta_{ij}^{\mathrm{eff}} l_{ij}}, \tag{2}$$

where r_{ij} and l_{ij} represent radius and length of pore throat ij, respectively, η_{ij}^{eff} is the local effective

dynamic viscosity of the fluid in the pore throat, which is a function of the shear rate in pore space, as well as the temperature, for a non-Newtonian fluid.

The dependence of the fluid's density on the temperature, T_i, was assumed to be given by,

$$\rho\left(T_i\right) = \rho\left(T_r\right) \exp\left[\beta\left(T_r - T_i\right)^m\right], \tag{3}$$

in which T_r is a reference temperature (usually assumed to be the critical temperature T_c of the fluid), and β and m are constant coefficients for a given chemical compound[57].

D. Heat Transfer

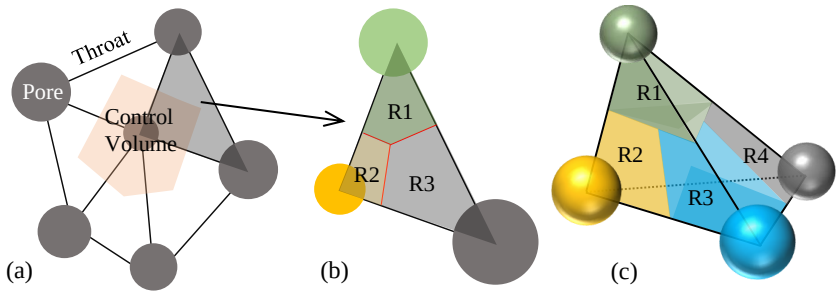

FIG. 2. (a) The 2D illustration of a control volume, including the solid and void space. (b) The solid space constrained between the pore throats is divided into three parts in 2D, R1, R2, and R3. The volume of each segment was approximated based on the volume of the connected pores. (c) The 3D graphic presentation of (b).

Heat transfer in saturated porous media occurs through both the fluid and solid phases. While heat transfer in the fluid is due to advection and diffusion (conduction), it is transferred through only conduction in the solid phase. For an unstructured 3D network, we propose a method for calculating the control volume of each control element, including a pore body, the connected throats, and the solid phase. The algorithm includes the following steps: (a) each pore body and the neighbouring pores were assumed to constitute a closed tetrahedron cell, using the Delaunay triangulation method; (b) the volume of the tetrahedron cells was calculated based on the locations of the connected pore bodies; (c) each cell was divided into four parts, the ratios of which depend on the volume of connected corner pores; (d) the control volume of each pore includes all the pieces from various directions; (e) the local porosity ϕ_{ij} was calculated using the local geometry as each control volume includes both the solid and void phase, as shown in Fig. 2(a); and (f)

the area of the interface connecting neighbouring control volumes was calculated by dividing the throat area by the local porosity. For a clear illustration, the formation of the control volume is shown in Fig. 2.

Local thermal equilibrium was assumed in each pore element, meaning that the temperature of the solid and fluid phases in each control volume were identical[58]. This is a valid assumption if the Biot number, Bi_i, is much smaller than 1 in a control volume.

$$\mathrm{Bi}_i = \frac{h_c}{\lambda_i^{\mathrm{sf}}} L = \frac{c_p^f \rho_i^f q_i T_i}{A_i^{\mathrm{sf}} \Delta T_i^{\mathrm{sf}} \lambda_i^{\mathrm{sf}}} L, \tag{4}$$

where h_c [W/(m^{2}K)] is the convective heat transfer coefficient, λ_i^{sf} [W/(m·K)] is the harmonic-averaged thermal conductivity of the solid and fluid phase, L [m] is the characteristic length assumed to be the apparent radius of the control element, c_p^f [J/(kg·K)] is the specific heat capacity of the flow-in fluid, ρ_i^f is the density of the fluid [kg/m^3], q_i [m^3/s] is the volume flux in the control volume i, A_i^{sf} [m^2] is the surface area between the fluid and the solid, T_i [K] represents the temperature of the injected fluid and ΔT_i^{sf} [K] is the temperature difference between the fluid and solid phases.

Under the assumption of local thermal equilibrium, thermal transport is simulated using the following equations, including thermal advection and diffusion in the porous media[59].

$$\rho_i^{\mathrm{eff}} V_i c_p^{\mathrm{eff}} \frac{\Delta T_i}{\Delta t} = -\sum_{q_{ij}>0} \rho_i^f |q_{ij}| c_p^f T_i + \sum_{q_{ij}<0} \rho_j^f c_p^f |q_{ij}| T_j + \sum_{j \in N_i} A_{ij}^{\mathrm{eff}} \lambda_{ij}^{\mathrm{eff}} \frac{T_j - T_i}{l_{ij}}, \tag{5}$$

where the left side of the equation is the rate of change of energy in control element i over a time step Δt, while the right side includes thermal advection by the fluid's velocity and thermal diffusion in both the solid and fluid phases. The fluid flux q_{ij} was estimated by the Hagen-Poiseuille equation, representing the volumetric flux from pore body i to pore body j. A_{ij}^{eff} is the cross-sectional area between connected pores, including both solid and fluid parts, while $\lambda_{ij}^{\mathrm{eff}}$ is the effective thermal conductivity.

The effective density ρ_i^{eff}, effective heat capacity c_p^{eff}, and the product of the effective thermal conductivity and effective area, $A_{ij}^{\mathrm{eff}} \lambda_{ij}^{\mathrm{eff}}$, were volume-averaged values of the solid and fluid phases based on the local porosity[22,60].

$$\rho_i^{\mathrm{eff}} = (1 - \phi_i)\, \rho_i^s + \phi_i \rho_i^f, \tag{6}$$

$$c_p^{\text{eff}} = \frac{(1-\phi_i)\,\rho_i^s c_p^s + \phi_i \rho_i^f c_p^f}{\rho_i^{\text{eff}}}, \tag{7}$$

$$A_{ij}^{\text{eff}} \lambda_{ij}^{\text{eff}} = \frac{1-\phi_{ij}}{\phi_{ij}} \pi r_{ij}^2 \lambda_s + \pi r_{ij}^2 \lambda_{ij}^f, \tag{8}$$

where superscripts s and f represent, respectively, the solid and fluid phase, A_{ij} is the cross-sectional area between the two control volumes including both the solid and fluid phases, and $\phi_{ij} = \left(\phi_i + \phi_j\right)/2$ is the average porosity of control volumes i and j.

If the Biot number is much larger than one[58], meaning that the local thermal equilibrium does not hold, two temperature distributions should be separately calculated for the fluid and solid phases, as shown by Eq. (9) and (10).

$$\begin{aligned} \rho_i^f V_i \phi_i c_p^f \frac{\Delta T_i^f}{\Delta t} = &- \sum_{q_{ij}>0} \left(\rho_i^f |q_{ij}| c_p^f T_i^f \right) + \sum_{q_{ij}<0} \left(\rho_j^f c_p^f |q_{ij}| T_j^f \right) + \\ &\sum_{j \in N_i} \left(A_{ij} \lambda_{ij}^f \frac{T_j^f - T_i^f}{l_{ij}} + A_i^{\text{sf}} \lambda_i^{\text{sf}} \frac{T_i^s - T_i^f}{R_i} \right) \end{aligned} \tag{9}$$

$$\rho_i^s V_i (1-\phi_i) c_p^s \frac{\Delta T_i^s}{\Delta t} = \sum_{j \in N_i} \left(A_{ij} \frac{1-\phi_{ij}}{\phi_{ij}} \lambda_{ij}^s \frac{T_j^s - T_i^s}{l_{ij}} + A_i^{\text{sf}} \lambda_i^{\text{sf}} \frac{T_i^f - T_i^s}{R_i} \right) \tag{10}$$

$$\lambda_i^{\text{sf}} = \frac{\lambda_i^f \lambda_i^s}{\lambda_i^f (1-\phi_i) + \lambda_i^s \phi_i} \tag{11}$$

where T_i^f and T_i^s are temperatures of the fluid and solid phases in the control volume i, R_i is the characteristic length of the control volume, A_i^{sf} is the interfacial area between the fluid and solid phases in control volume i, λ_i^{sf} is the harmonic-average thermal conductivity between the fluid and solid[61]. Note that Δt is the smallest time step, and that apart from the heat transfer between the neighbouring fluid and solid phases, the heat exchange in each control volume should also be calculated.

In the simulations, the solid phase was assumed to be sandstone, which is characteristically made of quartz. The density and thermal properties of sandstone were assumed to be independent of the temperatures, since the properties of sandstone are much less sensitive to temperature compared with the fluid. The density of sandstone was taken to be 2323 kg/m^3, its thermal conductivity was assumed to be $\lambda_s = 1.6$ W/(m·K), while its heat capacity was 672.62 J/(kg·K)[62].

E. Properties of the Non-Newtonian fluid

The viscosity of most shear-thinning and shear-thickening non-Newtonian fluids exhibits an S-shaped functional dependence on the shear stress τ. Such fluids behave as a Newtonian fluid, with their viscosity having a plateau at low and high values of τ, but a strong dependence on τ in the intermediate regime. The viscosity of non-Newtonian fluids also varies non-linearly with temperature. An equation that describes the S-shaped shear stress and temperature-dependent viscosity has not been reported in the literature. Thus, we modified the shear stress-dependent Meter equation to account for the temperature-dependent viscosity. The proposed equation could be referred to as thermal Meter equation (TME), Eq. (12), in order to distinguish it from the original Meter equation[32,63].

$$\begin{cases} \eta(\tau,T) = \eta_{\infty,T} + \frac{\eta_{0,T}-\eta_{\infty,T}}{1+\left(\tau/\tau_{m,T}\right)^{S_T}}, \\ \eta_{0,T} = \eta_{0,0}e^{-BT}, \\ \eta_{\infty,T} = \eta_{\infty,0}e^{-CT}, \\ \tau_{m,T} = \tau_{m,0}e^{DT}, \\ S_T = S_0 e^{ET}, \end{cases} \tag{12}$$

where $\eta(\tau,T)$ is the temperature- and shear stress- dependent viscosity of a non-Newtonian fluid at given shear stress τ and temperature T, $\eta_{0,T}$ and $\eta_{\infty,T}$ are the viscosity of the fluid at zero and infinite shear stresses, respectively, at temperature T, $\tau_{m,T}$ is shear stress of the fluid at a viscosity, $(\eta_{0,T}+\eta_{\infty,T})/2$ at temperature T_m, S_T is the shear stress-dependent exponent at a given temperature, $\eta_{0,0}$, $\eta_{\infty,0}$, $\tau_{m,0}$ and S_0 are the corresponding values at absolute zero temperature, and B, C, D and E are constants.

For a pore throat(i.e., cylindrical tube), the effective viscosity was calculated based on the following equation[63,64],

$$\eta(\tau,T) = \eta_{\infty,T} + \frac{\eta_{0,T}-\eta_{\infty,T}}{1+\left(\frac{\beta r_{ij}}{2\tau_{m,T}}\frac{\Delta P_{ij}}{l_{ij}}\right)^{S_T}}. \tag{13}$$

The parameters in Eq. (12) were estimated by fitting the equations to the experimental data for a given fluid. Then, the fitted parameters were used to calculate the effective viscosity using Eq. (13). In this paper, we simulated flow of a crude oil[65] to study thermal transport in flow of a non-Newtonian fluid in porous media. The dependence of the viscosity of non-Newtonian fluid on

the shear stress at various temperatures was fitted to data using the TME, and is shown in Fig. 3(a).

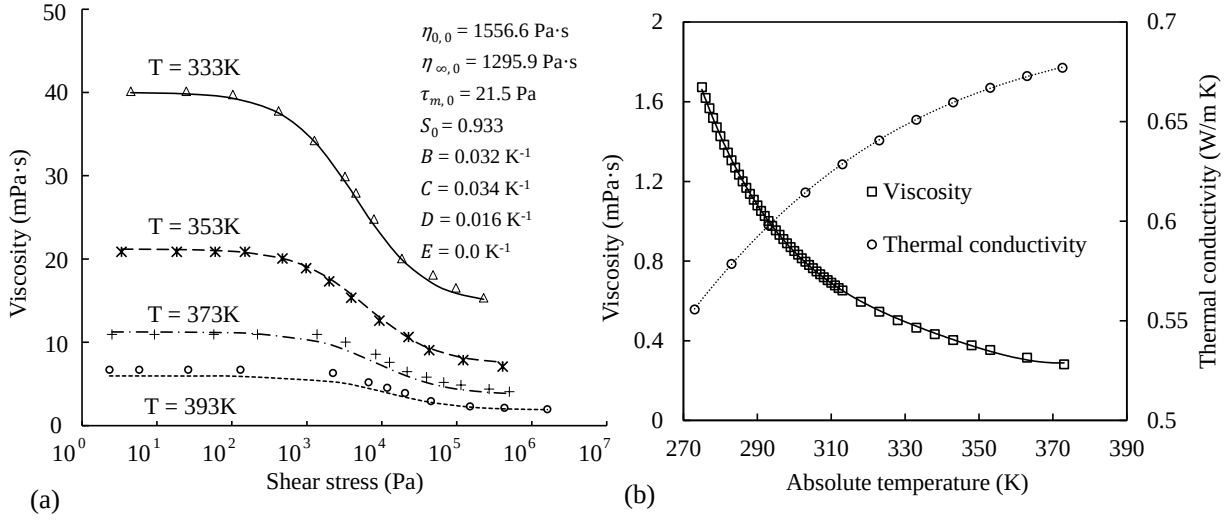

FIG. 3. (a) The relation between viscosity and the shear stress of the crude oil at various temperatures. The symbols represent experimental data, while the curves are the resulting fits. (b) Temperature-dependence of viscosity and thermal conductivity of water. Polynomial equations were fitted to the experimental data.

Change of heat capacity or thermal conductivity of non-Newtonian fluids (e.g., Xanthan gum solution) can be estimated by experiments. Otherwise, general empirical equations can be used to estimate the heat capacity as a function of temperature. The thermal conductivity of many liquid polymers increases with increasing temperature[66], and the increase is estimated based on Eq. (14).

$$\frac{1}{c_p^f}\frac{\mathrm{d}c_p^f}{\mathrm{d}T} \approx 1.0\times 10^{-3}\ \mathrm{K}^{-1}. \tag{14}$$

The thermal conductivity of liquid, λ_f, was estimated using the Weber equation[67]:

$$\lambda_f = 3.56\times 10^{-8} c_p^f \left(\frac{\rho^4}{M}\right)^{\frac{1}{3}}, \tag{15}$$

where M represents the molecular weight.

Due to the absence of accurate data, the heat capacity of the crude oil was assumed to be 2500 J/(kg·K) at the temperature of 298 K. The formulation of temperature- dependent heat capacity was derived based on Eq. (14), as

$$c_p^f = 2500 e^{0.001(T-298)}. \tag{16}$$

In the Weber equation, the molecular weight of the non-Newtonian fluid was assumed to be 250, while its density being the same as that of the chosen Newtonian fluid simulated in this paper (see below).

F. Properties of the Newtonian fluid

We assumed water to be the Newtonian fluid, whose flow and heat transfer were simulated through the pore space. The heat capacity of liquid water was assumed to be constant, 4200 J/(kg·K), when temperature was between 273 K and 373 K. The temperature-dependent density, viscosity, and thermal conductivity of liquid water were fitted using experimental data. Based on the Eq. (3), the fitted temperature-dependence of water density was determined to be, as $\rho\left(T_i\right) = 958.35\exp\left[0.001328\left(373-T_i\right)^{0.7943}\right]$. Using polynomial approximation, we fitted water density to the data, with the result being:

$$\eta = 3.40\times10^{-8}T^4 - 4.63\times10^{-5}T^3 + 2.37\times10^{-2}T^2 - 5.41T + 465.65. \tag{17}$$

If the temperature increases from 273 K to 373 K, the thermal conductivity of water increases slightly, as shown in Fig. 3(b). The experimental data were fitted using a polynomial approximation, with the result being,

$$\lambda_f = 4.07\times10^{-8}T^3 - 4.91\times10^{-5}T^2 + 2.01\times10^{-2}T - 2.10. \tag{18}$$

G. Computational setup and GPU-based acceleration

The spatially correlated and uncorrelated networks, governing equations for simulation, and properties of fluid and solid phases have been introduced as aforementioned. The networks were initially saturated by a fluid with temperature of 298 K. For boundary conditions, the fluid with temperature of 373 K was injected at the center of the radial domain with a constant flow rates, and the pores at outlet were assumed to be at atmospheric pressure. The flow simulation, heat transfer, and updating of the parameters, such as the density, viscosity, and thermal properties, were iteratively carried out. At time t, the temperature-dependent properties of the fluid were updated for the flow simulation. The computed pressure field was then utilized to update the viscosity in order to re-calculate the velocity field until the governing equations converged at time

t. Then, time was increased by time step Δt and heat transfer was simulated using Eq. (5) or Eqs. (9) and (10) to update the temperature field at time $t+\Delta t$.

To accelerate the computational speed and enlarge the simulation domain, flow and heat transfer simulations were fully parallelized using the GPU-CUDA technology[68,69]. A GPU-based linear solver based on Jacobi preconditioned conjugation gradient method was adopted to solve the mass balance equations, Eqs. (1) and (2)[27]. The governing equations for heat transfer through the porous medium were explicitly solved by allocating each element's equations into distinct threads. All the calculations were carried out on NVIDIA Tesla v100 GPU card, which had 5120 CUDA cores with 1380 MHz clock frequency, 900 GB/sec memory bandwidth, and 32 GB of global memory.

III. RESULTS AND DISCUSSIONS

A. Flow properties of the pore network

An uncorrelated network and a correlated one with a correlation length of 0.25 cm (1/20 of the system's radius) were generated. The absolute permeability of the uncorrelated and correlated networks were computed to be 0.25 D and 0.41 D, respectively, calculated based on Eq. (19).

$$Q = \frac{2\pi kh}{\eta_{\text{eff}} \ln\left(R_{\text{out}}/R_{\text{in}}\right)} \Delta P, \tag{19}$$

where Q is the volume flow rate, η_{eff} is the effective viscosity, R_{out} and R_{in} are the radii of inlet and outlet boundaries, respectively, h is the height of the sample, and ΔP is the pressure difference between the inlet and outlet.

The ratio of the thermal advection to diffusion (conduction) is referred to as Péclet number, defined as Eq. (20). The Péclet number was calculated under the initial temperature of 298 K.

$$Pe = \frac{uL}{\alpha} = \frac{Q(R_{\text{out}} - R_{\text{in}})\rho_{\text{eff}} c_p^{\text{eff}}}{2\pi R_{\text{out}} h \phi \lambda_{\text{eff}}}, \tag{20}$$

where $u = Q/\left(2\pi h R_{\text{out}}\phi\right)$ is the characteristic velocity at the outlet. Note that in a radial system such as one that we utilize, and with a constant injection rate, the radial velocity decreases with the distance from centre. $L = R_{\text{out}} - R_{\text{in}}$ is the characteristic length, and $\alpha = \lambda/\left(\rho c_p\right)$ is the thermal diffusivity. The averaged thermal diffusivity for bulk system was determined in as manner similar to Eqs. (6)-(8) using the porosity of the network.

B. Local thermal equilibrium versus non-equilibrium conditions

As already pointed out, the assumption of local thermal equilibrium is valid when the Biot number is much small than one[58]. As Eq. (4) indicates, the Biot number is directly proportional to the flow rate. At the highest flow rate that we simulated, 10.0 mm^3/s, we analyzed the distribution of local Biot number for each control volume for both Newtonian and non-Newtonian fluids in both correlated and uncorrelated networks. To calculate the Biot number under dynamic conditions, the thermal properties at the initial temperature were utilized to compute the velocity field. The temperature difference was taken to be the difference between the inlet and initial temperatures.

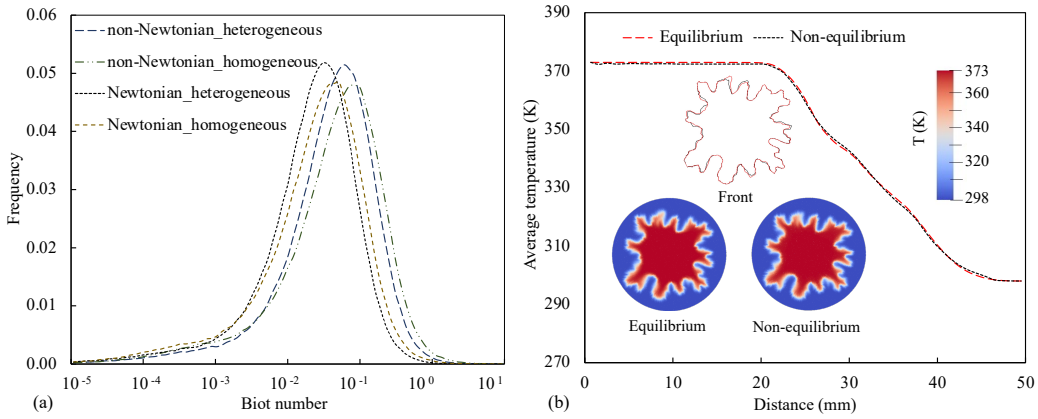

FIG. 4. (a) The distribution of local Biot numbers for the Newtonian (water) and non-Newtonian fluid (crude oil) under a flow rate of 10.0 mm^3/s in spatially homogeneous and heterogeneous networks. (b) The comparison of thermal patterns and average temperature under equilibrium (Eq 5) and non-equilibrium (Eqs. 9 and 10) conditions for the non-Newtonian fluid.

As shown in Fig. 4(a), a very small group of local Biot numbers are larger than 1, implying that the assumption of local thermal equilibrium is valid in all the simulations carried out. To assess further the impact of equilibrium assumption, using Eq. (5), on the upscaled behavior, non-Newtonian fluid flow in a spatially uncorrelated network at the highest volume flow rate was also simulated and compared with the non-equilibrium case, using Eqs. (9) and (10). The spatial temperature distribution and the dependence of the average temperature on the distance from center for the two cases at the breakthrough time are plotted in Fig. 4(b), which indicate almost identical fingering patterns and average cross-sectional temperature. Thus, in all the simulations, we assumed local thermal equilibrium.

For validation, to our knowledge, there is no experimental or theoretical work in literature for

transient non-isothermal flow of a non-Newtonian fluid through porous media in the literature, presumably due to experimental complexities. Therefore, we validated the model with isothermal non-Newtonian fluid flow experiments, as reported in Appendix A. The results there demonstrate that the pore-network model is capable of upscaling the rheology of fluid from bulk rheology to porous media rheology. To further validate the model under non-isothermal conditions, we propose an analytical solution for the location of thermal front in a spatially-uncorrelated pore network in order to compare the front from the numerical simulation, as shown in Appendix A. The dispersion was not considered in the analytical equation. Then, the effect of unstructured topology and heat transfer in solid phase were analyzed in Appendices B and C.

C. Effect of hydrodynamics and spatial heterogeneity on thermal fingering

We now present the results of our study of the effect of several factors on heat transfer in porous media, including (a) the flow rate (which is tantamount to varying the Péclet number), (b) Newtonian versus shear-thinning fluids, and (c) spatial heterogeneity by comparing the results for a spatially homogeneous network with those for a spatially correlated network but with same pore-size statistics.

To visually demonstrate and quantitatively analyze the results, all the analysis were carried out at the temperature breakthrough point, defined as the state when the temperature at the outlet is higher than its initial value. Flow rates of 0.01, 0.05, 0.1, 0.25, 0.5, 0.75, 1.0, 2.5, 5.0, and 10.0 mm^3/s were utilized in all the simulations. For water, these flow rates represented the Péclet numbers of 0.016, 0.082, 0.16, 0.41, 0.82, 1.23, 1.64, 4.11, 8.22 and 16.45, respectively. For the non-Newtonian fluid, based on the values of density, heat capacity and conductivity at the temperature of 298 K, the corresponding Péclet numbers were 0.026, 0.13, 0.27, 0.67, 1.33, 2.0, 2.67, 6.67, 13.36, and 26.72, respectively.

Newtonian fluid in a spatially homogeneous porous medium: As shown in the first row of Fig. 5(a), the temperature patterns at the breakthrough points are similar, in all direction, from the center to the outlet boundary for all the aforementioned flow rates. The reason is twofold: (a) the fluid is Newtonian, i.e., its viscosity is not sensitive to the shear stress and temperature, and (b) the medium is homogeneously random and no clear pathway was generated by the permeability field. With the increase of flow rate (i.e., increasing Péclet number), the transition front from maximum to minimum temperature becomes sharper due to the high intensity of advective transport.

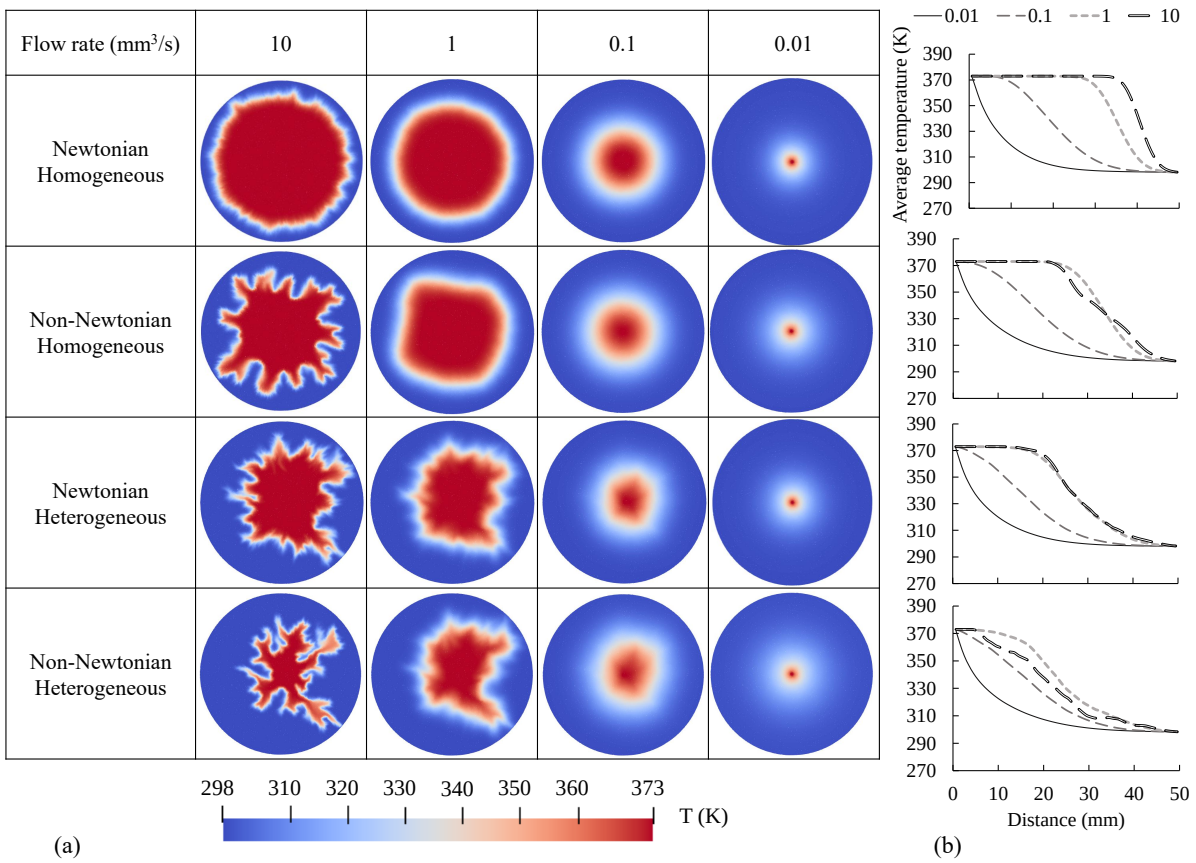

FIG. 5. (a) The thermal patterns at the breakthrough points of four cases, namely, Newtonian fluid in the uncorrelated porous medium, non-Newtonian fluid in the uncorrelated porous medium, Newtonian fluid in the correlated porous medium, and non-Newtonian fluid in the correlated porous medium under various injection flow rates. (b) The radially-averaged temperature from the inlet (center) to the outlet versus distance from the inlet.

The radially-averaged temperature versus distance from the center to the outlet boundary at the breakthrough point was calculated, as shown in Fig. 5(b). When thermal transport is dominated by diffusion, i.e., low Péclet number, for example, an injection flow rate of 0.01 mm^3/s, the temperature gradually decreases from the center toward the outlet, but the decreasing rate drops with the distance.

Shear-thinning fluid in a homogeneous porous medium: The second row of Fig. 5(a) shows the temperature field at the breakthrough point in the non-Newtonian shear-thinning fluid in the uncorrelated network (identical to the first row). Clearly, the decrease in the viscosity of the fluid associated with increased temperature and shear rates generated thermal fingering. For flow rates

smaller than 0.1 m^3/s, the thermal patterns are identical for both Newtonian and non-Newtonian fluid flow, since thermal diffusion governs heat transfer which is independent of the shear rate. When the flow rate is larger than 0.1 m^3/s, the effect of flow rate becomes clear as the fluid viscosity changes with the shear rates and thermal dispersion increases as well. Since the nature of the network in this case was spatially homogeneous, thermal fingering was generated in all directions.

Newtonian fluid in a heterogeneous porous medium: The third row of Fig. 5(a) indicates that thermal fingering in flow of the Newtonian fluid through a heterogeneous (spatially-correlated) network is far more visible than the homogeneous case. Due to the spatial correlation, clusters with large pores are connected together to generate the preferred paths for flow. Advection begins to control heat transfer when the injection flow rate is larger than 0.1 m^3/s, which results in the thermal fingering front. The radially-averaged temperature along the radius shown in Fig. 5(b), indicates that the heterogeneity clearly enhances the spreading of the temperature, and that even at high flow rates it is not possible to get a sharp transition in the temperature profile.

Shear-thinning fluid in a heterogeneous porous medium: Finally, the fourth row of Fig. 5(a) presents the combined effect of shearing-thinning behaviour and porous medium's heterogeneity on the temperature profile at the breakthrough point. The synergy of morphological heterogeneity and shear-thinning nature of fluid generated much clearer thermal fingering than the three previous cases. When the injection flow rate is smaller than 0.1 m^3/s, the transition from high to low temperature is smooth, with slight heterogeneity near the inlet. With increasing flow rate (i.e., increasing effect of advection), the thermal fingering pattern becomes more pronounced, especially for injection flow rates larger than 1.0 m^3/s. Clearly, the shear-thinning behaviour of the fluid, together with the heterogeneity enhance thermal fingering. Clusters of large pores in the correlated field generate the preferred flow and transport paths and, thus, the fluid has a higher velocity in such preferential pathways, which leads to reduction of fluid viscosity and enhancement of advective heat transfer. Thus, one expects shear-thickening fluid to behave completely different, and reduces the impact of the heterogeneity on thermal fingering, which is briefly studied in Appendix E. Therefore, using shear-thickening fluids, one can control thermal transport fingering in heterogeneous porous media.

Both morphological heterogeneity and shear-thinning nature of the fluid enhance thermal fingering in porous media. The thermal fingering patterns due to the two principal factors are, however, different. In the uncorrelated network, thermal fingering resulting from viscosity variations of

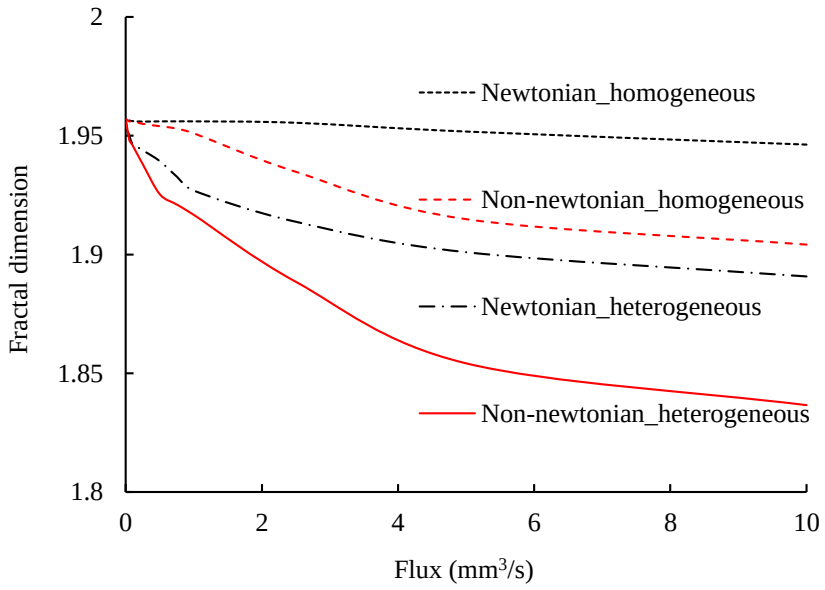

FIG. 6. Variation of the fractal dimension of the thermal front on the flow rate at the temperature breakthrough time. The network characteristics and shear-thinning properties are shown in Figs 1 and 3, respectively.

the fluid has a more smooth front and is randomly distributed in all directions. The heterogeneity-based thermal fingers, on the other hand, have preferred directions due to the structure of geometry. To quantitatively describe the complexity of the thermal morphology, the fractal dimension of thermal fronts was calculated using the box-counting method[70,71]. At the temperature breakthrough time, the fractal dimension of the thermal front was calculated. The depth was not considered in estimating the fractal dimension. As shown in Fig. 6, the fractal dimension decreases with the increase of the injection rate. For heat transfer in the Newtonian fluid through the uncorrelated network, the fractal dimension decreases slightly with the flow rate, and all the values are close to 2. The fractal dimensions for the other three cases have a more notable decrease. Note that the fractal dimension of thermal fingers is the smallest for the shear-thinning fluid in the correlated network.

The link between the microscale phenomena, such as the fingering pattern, and microscale heterogeneity with the upscaled properties can be made through the apparent viscosity, a lumped parameter that is significant for practical reasons. The average temperature and apparent viscosity of the Newtonian fluid for the entire domain at the breakthrough time were calculated and shown in Fig. 7(a). The same was also calculated for the non-Newtonian fluid and shown in Fig. 7(b).

For the Newtonian fluid, the relation between the average temperature and the flow rate exhibits an S-shape, ranging from diffusion-dominated to advection-dominated thermal transport. Correspondingly, the effective viscosity at the breakthrough point decreases with increasing flow rate (hence, the increased average temperature and shear rate).

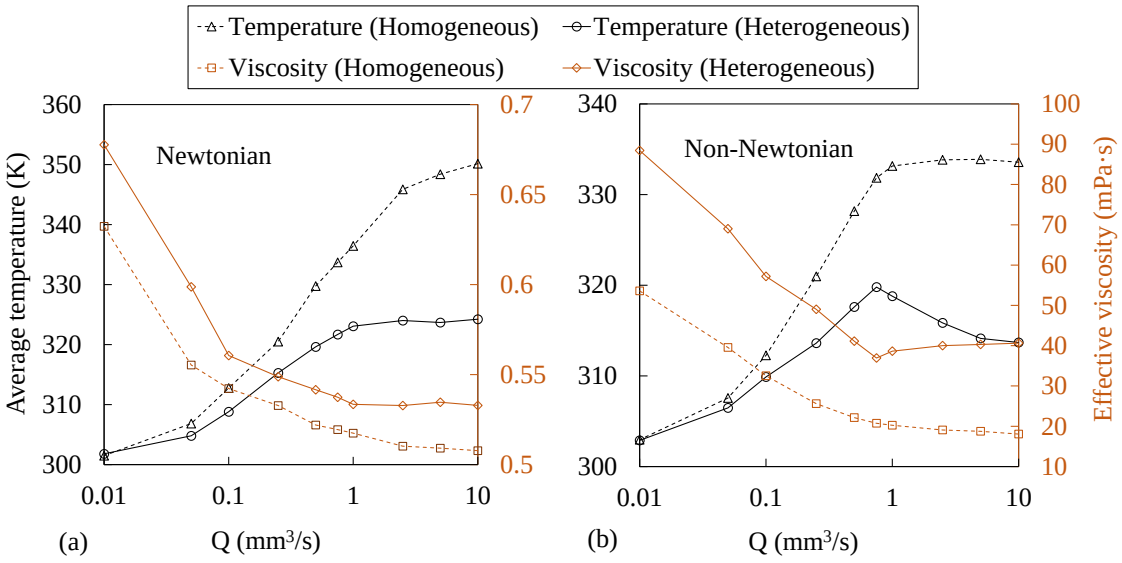

FIG. 7. The average temperature and effective viscosity at the breakthrough point for (a) the Newtonian fluid, and (b) the non-Newtonian fluid in uncorrelated and correlated networks with various injection flow rates.

For the non-Newtonian fluid in the spatially homogeneous network, shown in Fig. 7(b), the average temperature correlates positively with the flow rate up to 1.0 m^3/s, after which the average temperature slightly changes with the increase of flow rate. For the flow rates larger than 1.0 m^3/s, heat transfer is advection-dominated. Hence, further increase in the flow rates slightly enhances the broadness of the shear stress distribution in the pore space, and thus the fingering would be enhanced slightly. Due to increased advection, the radially-averaged temperature, shown in Fig. 5(b), also indicates that the location of the transition front decreased with increasing flow rate lower than 1.0 m^3/s, due to the increased advection. A wider front is, however, observed for flow rates larger than 1.0 m^3/s. Correspondingly, the apparent viscosity at the breakthrough point decreases with increasing flow rate up to 1.0 m^3/s. Afterward, the apparent viscosity is affected only weakly by the flow rate, due to limited spatial variability of the local viscosity.

The effect of spatial heterogeneity on average temperature is not significant at small flow rates, which is the diffusion-dominated region of thermal transport. With the formation of fingers at

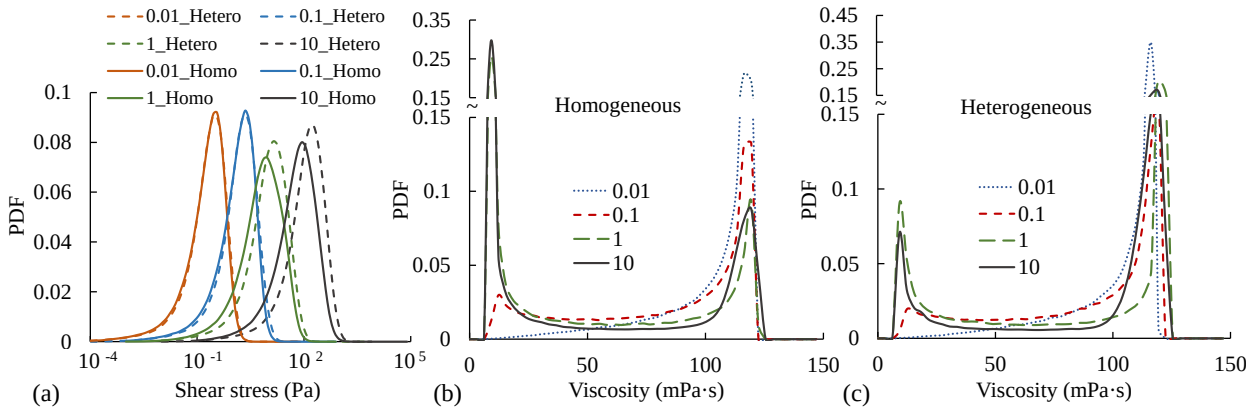

FIG. 8. The probability density functions of the pore-scale properties for injection flow rates from 0.01 to 10 mm^3/s at the breakthrough points, for (a) the shear stress, (b) viscosity in the spatially homogeneous network, and (c) viscosity in the heterogeneous network.

higher rates, however, the difference between average temperature in the spatially homogeneous and heterogeneous porous media is significant. Contrary to the aforementioned and described S-shape profile for the Newtonian fluid, the dependence of the average temperature and apparent viscosity on the flow rate exhibits non-monotonic behavior, shown in Fig. 7(b). By increasing the injection flow rate from 0.01 to 0.75 m^3/s, advection is enhanced but the diffusion still plays an important role by making the thermal pattern more uniform. In this range, the average temperature at the breakthrough point increases with the increasing flow rate. For flow rates larger than 0.75 m^3/s, thermal transport is controlled by advection, giving rise to specific thermal patterns. Moreover, increasing flow rate results in a further heterogeneous, fractal-like thermal pattern due to shear thinning. Correspondingly, the apparent viscosity reaches its lowest value at around the flow rate of 0.75 m^3/s. The transition length from the maximum temperature to the minimum value, shown in Fig. 5(b), becomes shorter with the increasing flow rate but smaller than 0.75 m^3/s, and then becomes longer because of the more nonuniform pattern of flow rates larger than 0.75 m^3/s.

To demonstrate the variations of shear stress and viscosity of the non-Newtonian fluid at pore-scale, their statistical distribution at the breakthrough time for injection flow rates, ranging from 0.01 mm^3/s to 10 mm^3/s, are shown in Fig. 8. Fig. 8(a) indicates that the shear stress of the non-Newtonian fluid increases with increasing injection rate, as expected. The difference between the spatially homogeneous and heterogeneous networks in terms of shear distribution is not significant, especially when the injection flow rate is less than 0.1 mm^3/s. On the other hand, heat transfer

is significantly influenced by the injection flow rate and the structure of the network, which led to significant variation in the pore-scale viscosity under various conditions, as shown in Fig. 8(b). For an injection flow rate of 0.01 mm^3/s, the smooth temperature pattern results in a monomodal distribution of the viscosity, regardless of the network heterogeneity. When advective transport becomes significant (with injection flow rate larger than 0.1 mm^3/s), a bimodal distribution of the pore-scale viscosity is developed. The small-viscosity peak represents the reduced viscosity due to the increased temperature and shear stress. The high-viscosity peak represents those parts of the domains that do not experience increased temperature. With increasing flow rate, the population of the intermediate pore-scale viscosities between two peaks decreases in size due to the decreasing ratio of the pores with transitional temperature (between the highest and lowest temperatures). Thus, the results imply that in such circumstances, the effect of temperature on the viscosity is much stronger than the corresponding effect of shear-thinning rheology for the chosen fluid properties and flow conditions. Further details are given in Appendix D. In the heterogeneous pore space, the fraction of pores with lower viscosities is smaller than that in the homogeneous network, which is caused by the stronger thermal fingering.

Our results imply that in the presence of heterogeneity and for a shear-thinning fluid, for applications such as thermal enhanced oil recovery, it is important to design the injection flow rates in a way that thermal fingering is minimized and a lower effective viscosity, similar to what Fig. 7(b) indicates, is achieved.

IV. CONCLUSIONS

To study thermal-viscous fingering instability in porous media, a pore network model and a computational algorithm were proposed in order to simulate time-dependent thermal transport in flow of a non-Newtonian fluid through 3D unstructured networks at centimeter level with millions of pores.

Both spatially-uncorrelated and correlated pore networks in a radial geometry were generated with identical pore-size distributions and topological structures. We also proposed a method for calculating the control volume of each pore body in the 3D unstructured networks. For the non-Newtonian fluid, a thermal Meter equation was proposed to express the relation between the viscosity and shear stress under varying temperatures. We then simulated the dynamics of coupled fluid flow and thermal transport for both Newtonian and non-Newtonian fluids under the assump-

tion of local thermal equilibrium. A simple analytical model, based on energy balance, for the position of thermal front in the radial geometry was also proposed. The fully GPU-parallelized algorithm made it possible to quickly carry out the simulation of thermal transport.

We analyzed the effect of the injection flow rate and heterogeneous morphology of the pore space on thermal transport and the resulting patterns for both Newtonian and non-Newtonian fluids. After comparing the thermal front obtained by numerical simulation with the predictions of the analytical model in a spatially uncorrelated network, the thermal patterns at the breakthrough point were analyzed for the Newtonian fluid, assumed to be water, and a crude oil that represented the non-Newtonian fluid, in both spatially heterogeneous and homogeneous porous media. Both the structural heterogeneity and the non-Newtonian nature of the fluid result in thermal-viscous fingering instability. The thermal fingers due to the heterogeneity have a preferred direction, reflecting the geometrical structure. Thermal fingering in the uncorrelated network due to the non-Newtonian rheology of the fluid and its associated shear rate-dependent viscosity propagate in all directions and with a smoother front. The fractal dimension of the thermal fronts indicates that the two phenomena enhance each other. For the flow of the Newtonian fluid in all networks, as well as the non-Newtonian fluid in the spatially-uncorrelated network, the dependence of the average temperature at the breakthrough point on the injection flow rate exhibits an S-shape form. For flow of a non-Newtonian fluid through a correlated porous medium the average temperature and the apparent viscosity follow non-monotonic dependence on increasing injection flow rates.

Appendix A: Validation against experiment and analytical model

For validation, to our knowledge, there is no experimental work in the literate that reports on transient non-Newtonian fluid flow under non-isothermal conditions, presumably due to experimental complexities. There have, however, been some experimental studies that were focused on isothermal non-Newtonian fluid flow through porous media. Thus, we validated our model with the experimental data reported in Eberhard *et al.*[72]. The porous medium was made of packed monodisperse spherical beads.

The network was extracted from the generated packed bed, shown in Fig. 9(a). To accurately fit the absolute permeability of the bead packing using the pore-network model, the pore sizes were increased by a factor of 1.07. The measured bulk rheology was fitted using the MMM as shown in Fig 9(b). With the bulk rheology data and pore-network morphology, the non-Newtonian fluid

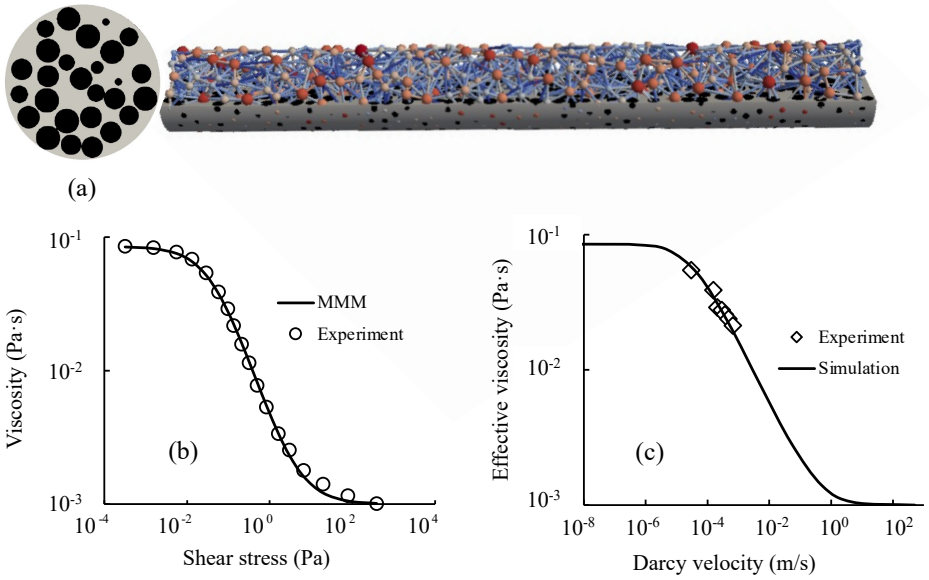

FIG. 9. (a) A randomly packed bed of monodisperse spherical beads and extracted pore network. Details about the sample can be found in Eberhard *et al.*[72]. (b) Fitted rheology using MMM. (c) Comparison between simulation results and experimental data.

flow in the pore network was simulated under isothermal condition using various injection rates. As a result, we established the relation between the Darcy velocity and effective viscosity of the non-Newtonian fluid flow through the porous medium, and compared the results with experimental data as shown in Fig. 9(c). The results clearly demonstrate that the model is capable of reproducing the experimental data.

Given that we perform simulation for non-isothermal conditions, we wish to demonstrate the effect of heat exchange between the solid and the fluids and the change of rheology due to the non-isothermal effects. Thus, we propose a simplified analytical solution for the location of thermal front, by excluding dispersion, in a spatially-uncorrelated pore network in order to compare the front compared by the numerical simulation, as shown in Appendix A. The energy balance was checked for all the simulations by comparing thermal energy entering and leaving the system, i.e., $E_{\text{in}} - E_{\text{out}}$, versus additional internal energy E_{add} in the entire domain Ω.

$$\Delta E = E_{\text{in}} - E_{\text{out}} = \int_0^t Q_{\text{in}} \rho_f c_p^f (T_{\text{in}} - T_{\text{out}})\, \mathrm{d}t, \tag{A1}$$

$$E_{\text{add}} = \sum_{i\in\Omega} \left[(1-\phi_i) V_i \rho_s c_p^s + \phi_i V_i \rho_{fi} c_{pi}^f \right] (T_i - T_0). \tag{A2}$$

The quantitative relative error was less than 0.01 percent for energy balance in all the simulations. Additionally, for further assessment, an analytical expression for thermal front, Eq. (A4), is proposed to compare its prediction against the simulation results. To be able to use the analytical expression, the densities and heat capacities of the fluids and the solid phase were assumed to be constant (values taken at 298 K).

The energy storage capacity of the water-saturated network was calculated based on,

$$C_{\text{tol}} = (1-\phi) V \rho_s c_p^s + \phi V \rho_f c_p^f. \tag{A3}$$

We set the constant boundary flux at Q_{in} = 10.0 mm^3/s at the inlet boundary (center of the system). The initial temperature of the porous medium was 298 K, and the injected fluid had a constant temperature of T_{in} = 373 K. The temperature of system near the inlet boundary quickly increased to 373 K. Thus, the energy contributed by diffusion between the injected fluid and the inlet pore units was ignored, meaning all the in-flow energy (E_{in}) in the domain is due to convection. The energy adding rate, defined as the difference between in-flow and out-flow energy (E_{out}), was calculated using Eq. (A1). Assuming a sharp thermal front in the spatially homogeneous porous medium, the front location is calculated by,

$$\begin{aligned} L_f &= \sqrt{\frac{\Delta E}{C_{\text{tol}}(T_{\text{in}} - T_0)} \left(R_{\text{out}}^2 - R_{\text{in}}^2\right) + R_{\text{in}}^2} \\ &= \sqrt{\frac{Q_{\text{in}} \rho_f c_p^f t}{(1-\phi) V \rho_s c_p^s + \phi V \rho_f c_p^f} \left(R_{\text{out}}^2 - R_{\text{in}}^2\right) + R_{\text{in}}^2}, \end{aligned} \tag{A4}$$

where L_f represents the front location (radial distance from the center), and ϕ and V represent the porosity and bulk volume of the network, respectively.

The porosity of the uncorrelated network was about 0.184. Therefore, energy storage capacity of the water-saturated network, C_{tol}, turned out to be 1.61 J/K. So long as the temperature of the outlet pores was higher than the initial temperature (T_{out} = 298K), we had ΔE = 3.15 J/s. For the uncorrelated network, the front locations were calculated using Eq. (A4) at a given time, represented by the vertical solid lines in Fig. 10(b). Since the porous media have a distribution of the pore sizes, they lead to a distribution of advective force and thermal dispersion. Thus, the

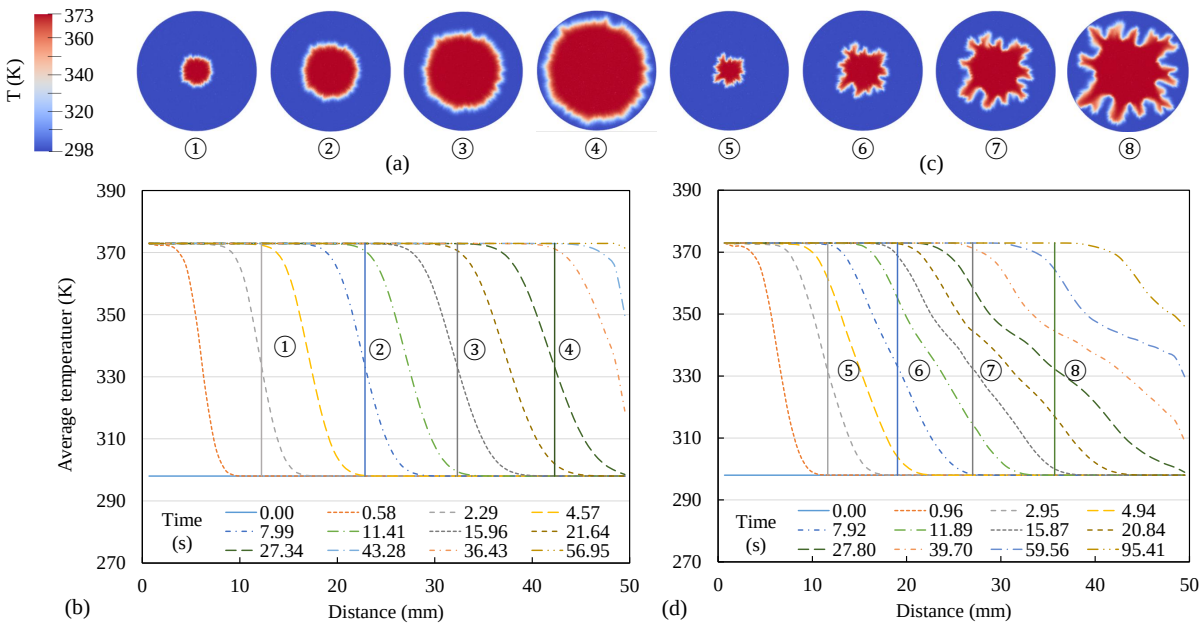

FIG. 10. Dynamic evolution temperature in (a) the Newtonian and (c) non-Newtonian fluids. The performance of the analytical expression for purely advective heat transfer based on Eq. (A4) (vertical lines), is compared with the average front temperature obtained by simulations for (b) Newtonian and (d) non-Newtonian fluids.

temperature profiles in porous media are not similar to a step function. The middle point of the smeared front represents the purely advective heat transfer (without dispersion) that is presented in Fig. 10(b). With the same boundary conditions as before, we simulated the flow of crude oil and heat transfer in the identical uncorrelated network. As shown in Fig. 10(c), the transition front for the crude oil with shear-thinning properties is much longer than that of water. We also estimated the average front location by Eq. (A4), shown as the vertical lines in Fig. 10(d). Clearly, the analytical equation failed to accurately predict thermal fingering in non-Newtonian heat transfer in the porous medium studied.

Appendix B: Comparison of thermal fingering in 3D structured and unstructured networks

To compare the effect of a structured and unstructured morphology on heat transfer in flow through the pore networks, we generated both networks with volume of 1 cm^3. The spatial correlation length in the correlated network was 1/20 of its linear size, as shown in Fig. 11. The uncorrelated networks, shown in Figs. 11(a) and (b), had identical pore-size distribution pattern.

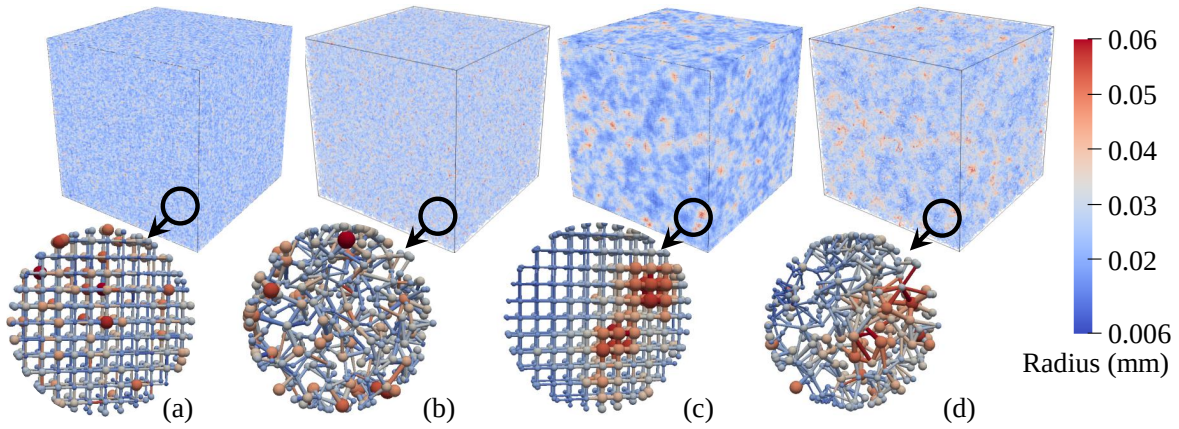

FIG. 11. (a) The structured and uncorrelated networks, (b) the unstructured and uncorrelated network, (c) the structured and correlated network, and (d) the unstructured and correlated network.

The radius of correlated networks, shown in Figs. 11(c) and (d), are also assigned based on the same radius field. To guarantee that heat transfer is simulated in the networks with the same absolute permeability, the pore sizes of the structured network were re-scaled using a scaling factor of 0.91. The absolute permeabilities of uncorrelated and correlated networks were 138 and 145 mD, respectively. The thermal pattern and average distribution of temperatures were analyzed for four networks saturated with the non-Newtonian fluid, shown in Fig. 12. Although the structured networks could produce qualitatively the temperature patterns, the upscaled properties do have clear difference with those of the unstructured networks, especially the change between uncorrelated and correlated networks.

Appendix C: Effect of solid phase on heat transfer

To indicate the importance of accurate simulation of heat transfer between the fluid and solid phases, we compare the simulation results with and without heat transfer in the solid phase, as shown in Fig. 13. Based on the temperature field at the breakthrough time, we conclude that heat transfer only in the fluid phase fails to predict the dynamic thermal front, as the heat capacity and conductivity are highly dependent on the solid ratio of each control volume.

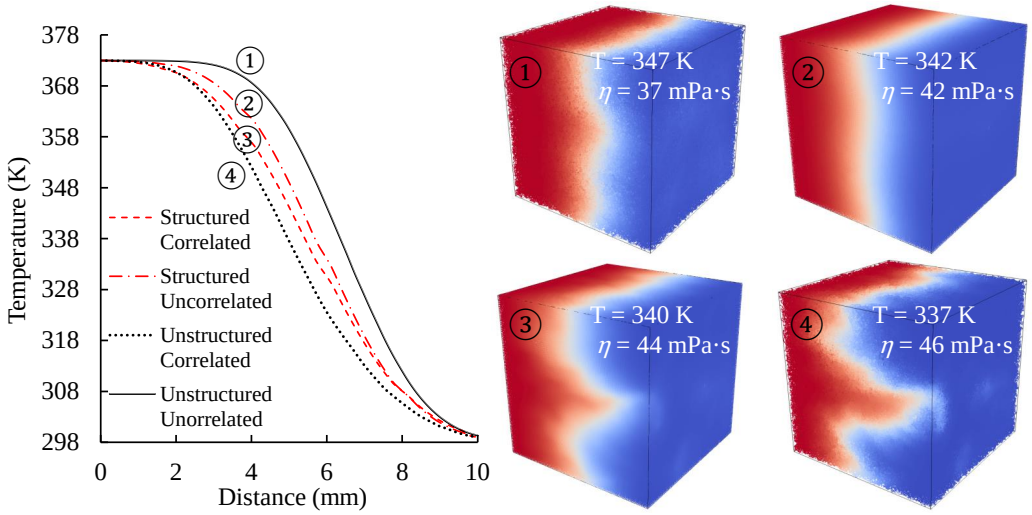

FIG. 12. Temperature distribution at the breakthrough time in networks with an injection flow rate of 10.0 mm^3/s, corresponding to the cases shown in Fig. 11.

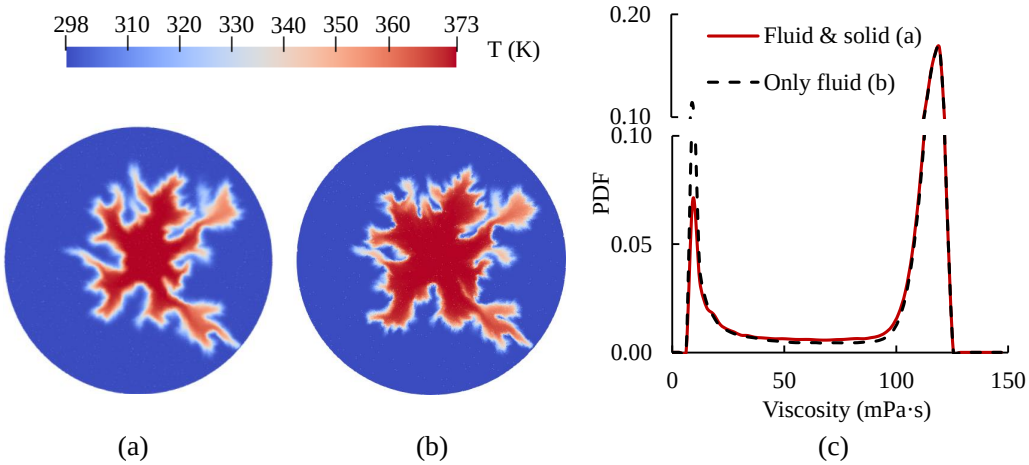

FIG. 13. The temperature distribution at breakthrough time in the spatially correlated network under flow rate of 10.0 mm^3/s with heat transfer (a) in both solid and fluid phases and (b) only in fluid phase. (c) The comparison of the local viscosity distribution in the two systems.

Appendix D: Effect of temperature- and shear-dependent viscosity on thermal fingering

For the non-Newtonian fluid, the effect of temperature- and shear-dependent viscosity on thermal fingering was studied with an injection flow rate of 1.0 mm^3/s. The comparison indicates that

the effect of temperature on thermal fingering is much stronger than the rheology of the shear-thinning fluid under the flow conditions that we simulated.

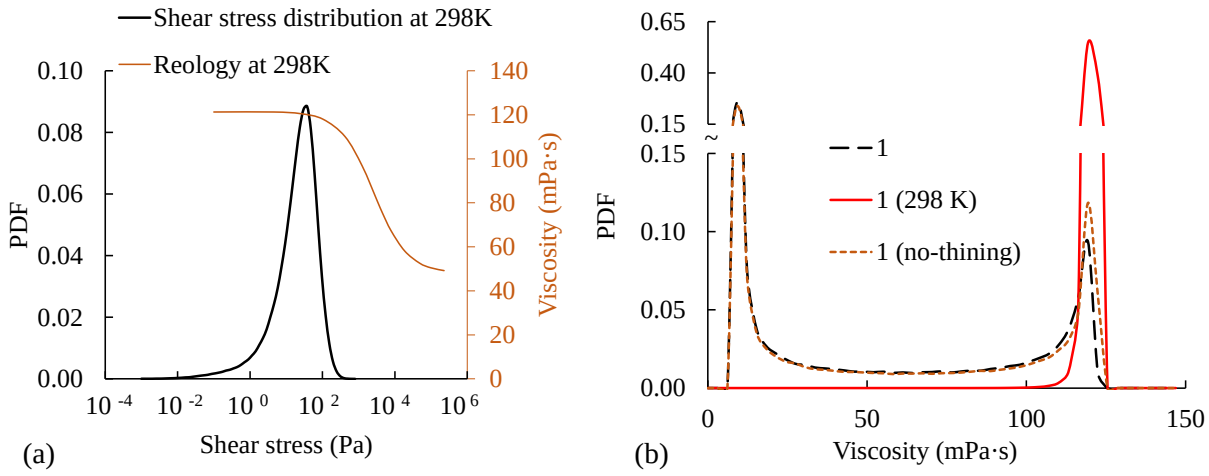

FIG. 14. (a) Rheology of the non-Newtonian fluid under the temperature of 298 K, and the distribution of the local shear stress with an injection flow rate of 1.0 mm^3/s. (b) The comparison of the local viscosity distribution under three conditions, namely, 1) the temperature- and shear-dependent viscosity, 2) the shear-dependent viscosity under the temperature of 298 K, and 3) the temperature-dependent viscosity ignoring shear-thinning property.

Appendix E: Comparison between shear-thinning and shear thickening fluid

In the present work, the results are based on a shear-thinning fluid. We anticipate that the rheology of shear-thickening fluids should reduce the impact of the heterogeneity on thermal fingering. Thus, we simply generated two inverted rheologies and simulated heat transfer in two fluids, assuming that the viscosity is dependent on the shear stress. The temperature fields and corresponding distributions of local shear stress and viscosity are shown in Fig. 15. The average temperature under the conditions of Fig. 15(a) is 324.9 K, and 330.4 K for Fig. 15(b). The fields are binarized using a threshold of median temperature. Then the fractal dimension was calculated for the binary images, obtaining 1.891 and 1.922, respectively. Thus, the simulations indicate that shear-thickening rheology weakens the fingering.

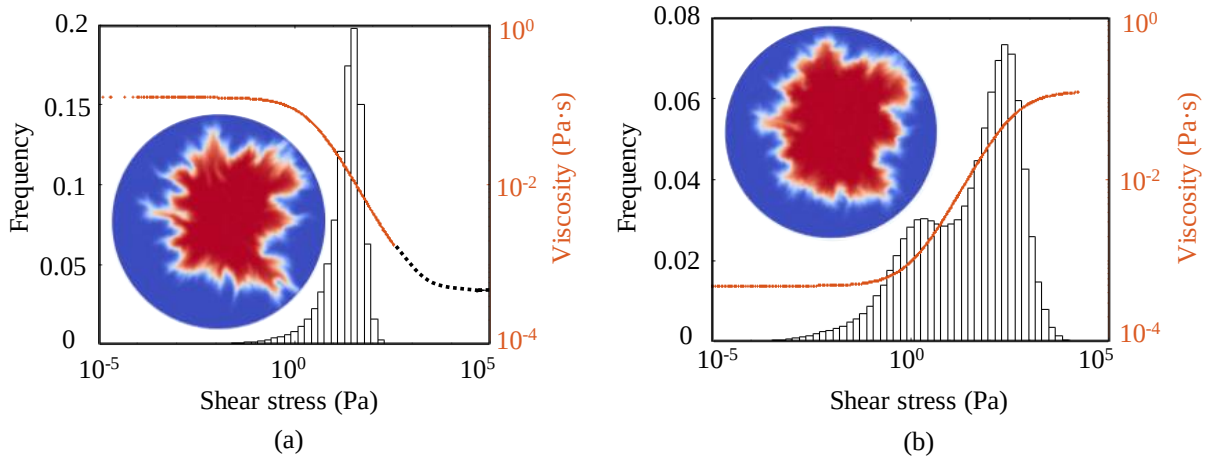

FIG. 15. Temperature fields, and the distribution of local shear stress and viscosity in pore throats of (a) shear-thinning fluid and (b) shear-thickening fluid.

ACKNOWLEDGMENTS

This research was supported by the President's Doctoral Scholar Award of the University of Manchester.

AUTHORS' CONTRIBUTIONS

The project and its objectives were designed by VN, SA, and MS. SA developed the computational codes, performed the simulations and analysis. TS, SA, and MB developed the non-Newtonian rheological model, Eq. (12). The first draft was jointly written by SA and VN, followed by contributions by the other authors to produce the final draft, while the final draft was edited by MS.

DATA AVAILABILITY STATEMENT

The data supporting the findings of this study are available from the corresponding author upon request.

REFERENCES

[1]B. Marsh and L. Kantha, "On the heat and mass transfer from an ascending magma," Earth and Planetary Science Letters **39**, 435–443 (1978).

[2]A. K. Schindler and K. J. Folliard, "Influence of supplementary cementing materials on the heat of hydration of concrete," in *Advances in Cement and Concrete IX Conference, Copper Mountain Conference Resort in Colorado* (2003).

[3]R. M. Butler, *Thermal recovery of oil and bitumen* (Old Tappan, NJ (United States); Prentice Hall Inc., 1991).

[4]A. M. Papadopoulos, "State of the art in thermal insulation materials and aims for future developments," Energy and buildings **37**, 77–86 (2005).

[5]A. I. Tok, F. Y. Boey, and Y. Lam, "Non-Newtonian fluid flow model for ceramic tape casting," Materials Science and Engineering: A **280**, 282–288 (2000).

[6]M. SHIRATO, T. ARAGAKI, and E. IRITANI, "Analysis of constant pressure filtration of power-law non-Newtonian fluids," Journal of Chemical Engineering of Japan **13**, 61–66 (1980).

[7]B. Straubhaar, J. Pauchet, and M. Prat, "Pore network modelling of condensation in gas diffusion layers of proton exchange membrane fuel cells," International Journal of Heat and Mass Transfer **102**, 891–901 (2016).

[8]D. Or, P. Lehmann, E. Shahraeeni, and N. Shokri, "Advances in soil evaporation physics—a review," Vadose Zone Journal **12**, 1–16 (2013).

[9]J. Cobeña-Reyes and M. Sahimi, "Rheology of water in small nanotubes," Physical Review E **102**, 023106 (2020).

[10]I. Ataei-Dadavi, N. Rounaghi, M. Chakkingal, S. Kenjeres, C. R. Kleijn, and M. J. Tummers, "An experimental study of flow and heat transfer in a differentially side heated cavity filled with coarse porous media," International Journal of Heat and Mass Transfer **143**, 118591 (2019).

[11]J. Beck and A. Beck, "Computing thermal conductivities of rocks from chips and conventional specimens," Journal of Geophysical Research **70**, 5227–5239 (1965).

[12]F. Tong, L. Jing, and R. W. Zimmerman, "An effective thermal conductivity model of geological porous media for coupled thermo-hydro-mechanical systems with multiphase flow," International Journal of Rock Mechanics and Mining Sciences **46**, 1358–1369 (2009).

[13]S. Torquato and H. Haslach Jr, "Random heterogeneous materials: microstructure and macroscopic properties," Appl. Mech. Rev. **55**, B62–B63 (2002).

[14]K. Vafai, S. J. Kim, *et al.*, "Forced convection in a channel filled with a porous medium: an exact solution," ASME J. Heat Transfer **111**, 1103–1106 (1989).

[15]W. Lu, C. Zhao, and S. Tassou, "Thermal analysis on metal-foam filled heat exchangers. Part i: Metal-foam filled pipes," International journal of heat and mass transfer **49**, 2751–2761 (2006).

[16]H. Xu, C. Zhao, and K. Vafai, "Analytical study of flow and heat transfer in an annular porous medium subject to asymmetrical heat fluxes," Heat and Mass Transfer **53**, 2663–2676 (2017).

[17]K. Vafai and C. L. Tien, "Boundary and inertia effects on flow and heat transfer in porous media," International Journal of Heat and Mass Transfer **24**, 195–203 (1981).

[18]Z. Guo and T. Zhao, "A lattice Boltzmann model for convection heat transfer in porous media," Numerical Heat Transfer, Part B **47**, 157–177 (2005).

[19]D. Gao, Z. Chen, and L. Chen, "A thermal lattice Boltzmann model for natural convection in porous media under local thermal non-equilibrium conditions," International Journal of Heat and Mass Transfer **70**, 979–989 (2014).

[20]B. Markicevic, A. Bazylak, and N. Djilali, "Determination of transport parameters for multi-phase flow in porous gas diffusion electrodes using a capillary network model," Journal of Power Sources **171**, 706–717 (2007).

[21]E. F. Médici and J. S. Allen, "Evaporation, two phase flow, and thermal transport in porous media with application to low-temperature fuel cells," International Journal of Heat and Mass Transfer **65**, 779–788 (2013).

[22]K. H. Le, A. Kharaghani, C. Kirsch, and E. Tsotsas, "Pore network simulations of heat and mass transfer inside an unsaturated capillary porous wick in the dry-out regime," Transport in porous media **114**, 623–648 (2016).

[23]V. Surasani, T. Metzger, and E. Tsotsas, "A non-isothermal pore network drying model with gravity effect," Transport in porous media **80**, 431–439 (2009).

[24]V. Surasani, T. Metzger, and E. Tsotsas, "Drying simulations of various 3d pore structures by a nonisothermal pore network model," Drying Technology **28**, 615–623 (2010).

[25]N. Belgacem, M. Prat, and J. Pauchet, "Coupled continuum and condensation–evaporation pore network model of the cathode in polymer-electrolyte fuel cell," International Journal of Hydrogen Energy **42**, 8150–8165 (2017).

[26]T. Koch, K. Weishaupt, J. Müller, B. Weigand, and R. Helmig, "A (dual) network model for heat transfer in porous media," Transport in Porous Media , 1–35 (2021).

[27]S. An, S. Hasan, H. Erfani, M. Babaei, and V. Niasar, "Unravelling effects of the pore-size correlation length on the two-phase flow and solute transport properties; GPU-based pore-network modelling," Water Resources Research , e2020WR027403 (2020).

[28]A. Metzner and R. Otto, "Agitation of non-Newtonian fluids," AIChE Journal **3**, 3–10 (1957).

[29]R. Rebhi, M. Mamou, and N. Hadidi, "Bistability bifurcation phenomenon induced by non-newtonian fluids rheology and thermosolutal convection in rayleigh–bénard convection," Physics of Fluids **33**, 073104 (2021).

[30]M. M. Cross, "Rheology of non-Newtonian fluids: a new flow equation for pseudoplastic systems," Journal of colloid science **20**, 417–437 (1965).

[31]K. Yasuda, *Investigation of the analogies between viscometric and linear viscoelastic properties of polystyrene fluids*, Ph.D. thesis, Massachusetts Institute of Technology (1979).

[32]D. M. Meter and R. B. Bird, "Tube flow of non-Newtonian polymer solutions: Part i. laminar flow and rheological models," AIChE Journal **10**, 878–881 (1964).

[33]K. Sorbie, P. Clifford, and E. Jones, "The rheology of pseudoplastic fluids in porous media using network modeling," Journal of Colloid and Interface Science **130**, 508–534 (1989).

[34]J. Pearson and P. Tardy, "Models for flow of non-Newtonian and complex fluids through porous media," Journal of Non-Newtonian Fluid Mechanics **102**, 447–473 (2002).

[35]C. L. Perrin, P. M. Tardy, K. S. Sorbie, and J. C. Crawshaw, "Experimental and modeling study of Newtonian and non-Newtonian fluid flow in pore network micromodels," Journal of Colloid and Interface Science **295**, 542–550 (2006).

[36]X. Lopez, P. H. Valvatne, and M. J. Blunt, "Predictive network modeling of single-phase non-Newtonian flow in porous media," Journal of colloid and interface science **264**, 256–265 (2003).

[37]T. Sochi, "Non-Newtonian flow in porous media," Polymer **51**, 5007–5023 (2010).

[38]M. Balhoff, D. Sanchez-Rivera, A. Kwok, Y. Mehmani, and M. Prodanović, "Numerical algorithms for network modeling of yield stress and other non-Newtonian fluids in porous media," Transport in porous media **93**, 363–379 (2012).

[39]S. Aghabozorgi and B. Rostami, "An investigation of polymer adsorption in porous media using pore network modelling," Transport in Porous Media **115**, 169–187 (2016).

[40]F. Xiong, W. Sun, J. Ba, and J. M. Carcione, "Effects of fluid rheology and pore connectivity on rock permeability based on a network model," Journal of Geophysical Research: Solid Earth **125**, no–no (2020).

[41]P. G. Saffman and G. I. Taylor, "The penetration of a fluid into a porous medium or Hele-Shaw cell containing a more viscous liquid," Proceedings of the Royal Society of London. Series A. Mathematical and Physical Sciences **245**, 312–329 (1958).

[42]G. M. Homsy, "Viscous fingering in porous media," Annual review of fluid mechanics **19**, 271–311 (1987).

[43]X. Kong, M. Haghighi, and Y. Yortsos, "Visualization of steam displacement of heavy oils in a Hele-Shaw cell," Fuel **71**, 1465–1471 (1992).

[44]K. Sasaki, A. Satoshi, N. Yazawa, F. Kaneko, *et al.*, "Microscopic visualization with high resolution optical-fiber scope at steam chamber interface on initial stage of SAGD process," in *SPE/DOE Improved Oil Recovery Symposium* (Society of Petroleum Engineers, 2002).

[45]T. W. de Haas, H. Fadaei, U. Guerrero, and D. Sinton, "Steam-on-a-chip for oil recovery: the role of alkaline additives in steam assisted gravity drainage," Lab on a Chip **13**, 3832–3839 (2013).

[46]A. H. Syed, N. Mosavat, J. Riordon, P. Lele, Z. Qi, M. Kim, H. Fadaei, A. Guerrero, and D. Sinton, "A combined method for pore-scale optical and thermal characterization of SAGD," Journal of Petroleum Science and Engineering **146**, 866–873 (2016).

[47]J. Cui and T. Babadagli, "Retrieval of solvent injected during heavy-oil recovery: Pore scale micromodel experiments at variable temperature conditions," International Journal of Heat and Mass Transfer **112**, 837–849 (2017).

[48]Y. Wang, H. Liu, Q. Zhang, Z. Chen, J. Wang, X. Dong, and F. Chen, "Pore-scale experimental study on EOR mechanisms of combining thermal and chemical flooding in heavy oil reservoirs," Journal of Petroleum Science and Engineering **185**, 106649 (2020).

[49]J. Kuang, T. Maxworthy, and P. Petitjeans, "Miscible displacements between silicone oils in capillary tubes," European Journal of Mechanics-B/Fluids **22**, 271–277 (2003).

[50]K. E. Holloway and J. R. De Bruyn, "Viscous fingering with a single fluid," Canadian Journal of Physics **83**, 551–564 (2005).

[51]Y. Nagatsu, N. Fujita, Y. Kato, and Y. Tada, "An experimental study of non-isothermal miscible displacements in a Hele-Shaw cell," Experimental thermal and fluid science **33**, 695–705 (2009).

[52]M. Islam and J. Azaiez, "Miscible thermo-viscous fingering instability in porous media. Part 1: Linear stability analysis," Transport in porous media **84**, 821–844 (2010).

[53]M. Norouzi, S. Dorrani, H. Shokri, and O. A. Bég, "Effects of viscous dissipation on miscible thermo-viscous fingering instability in porous media," International Journal of Heat and Mass

Transfer **129**, 212–223 (2019).

[54]M. Shabouei and K. Nakshatrala, "On numerical stabilization in modeling double-diffusive viscous fingering," Transport in Porous Media **132**, 39–52 (2020).

[55]D. Kinniment and E. Chester, "Design of an on-chip random number generator using metastability," in *Proceedings of the 28th European Solid-State Circuits Conference* (IEEE, 2002) pp. 595–598.

[56]V. Joekar-Niasar and S. Hassanizadeh, "Analysis of fundamentals of two-phase flow in porous media using dynamic pore-network models: A review," Critical reviews in environmental science and technology **42**, 1895–1976 (2012).

[57]A. K. Coker, *Ludwig's Applied Process Design for Chemical and Petrochemical Plants (Fourth Edition)* (Gulf Professional Publishing, 2007) pp. 103–132.

[58]F. P. Incropera, A. S. Lavine, T. L. Bergman, and D. P. DeWitt, *Fundamentals of heat and mass transfer* (Wiley, 2007).

[59]J. L. Vázquez, *The porous medium equation: mathematical theory* (Oxford University Press on Demand, 2007).

[60]E. Tsotsas and H. Martin, "Thermal conductivity of packed beds: a review," Chemical Engineering and Processing: Process Intensification **22**, 19–37 (1987).

[61]C. Wang and P. J. Fox, "Analytical solutions for heat transfer in saturated soil with effective porosity," Journal of Geotechnical and Geoenvironmental Engineering **146**, 04020095 (2020).

[62]D. Koňáková, E. Vejmelková, and R. Černỳ, "Thermal properties of selected sandstones," in *Advances in modern mechanical engineering: Proceedings of the 4th International Conference on Fluid Mechanics and Heat & Mass Transfer (FLUIDSHEAT'13), Dubrovnik, Croatia, 25–27 June 2013*. (2013) pp. 100–104.

[63]T. Shende, V. J. Niasar, and M. Babaei, "Effective viscosity and reynolds number of non-Newtonian fluids using meter model," Rheologica Acta **60**, 11–21 (2021).

[64]T. Shende, V. Niasar, and M. Babaei, "Upscaling non-Newtonian rheological fluid properties from pore-scale to Darcy's scale," Chemical Engineering Science **239**, 116638 (2021).

[65]N. Marx, L. Fernández, F. Barceló, and H. Spikes, "Shear thinning and hydrodynamic friction of viscosity modifier-containing oils. Part i: shear thinning behaviour," Tribology Letters **66**, 92 (2018).

[66]S. Kasap and P. Capper, *Springer handbook of electronic and photonic materials (Chapter 19)* (Springer, 2017).

[67]H. Weber, "Investigations into the thermal conductivity of liquids," Wiedemanns Annalen der Physik und Chimie **10**, 103 (1880).

[68]S. An, H. W. Yu, and J. Yao, "GPU-accelerated volumetric lattice Boltzmann method for porous media flow," Journal of Petroleum Science and Engineering **156**, 546–552 (2017).

[69]S. An, H. W. Yu, Z. Wang, B. Kapadia, and J. Yao, "Unified mesoscopic modeling and GPU-accelerated computational method for image-based pore-scale porous media flows," International Journal of Heat and Mass Transfer **115**, 1192–1202 (2017).

[70]K. Foroutan-pour, P. Dutilleul, and D. L. Smith, "Advances in the implementation of the box-counting method of fractal dimension estimation," Applied mathematics and computation **105**, 195–210 (1999).

[71]M. Sahimi, *Heterogeneous Materials I: Linear transport and optical properties*, Vol. 22 (Springer Science & Business Media, 2003).

[72]U. Eberhard, H. J. Seybold, M. Floriancic, P. Bertsch, J. Jiménez-Martínez, J. S. Andrade Jr, and M. Holzner, "Determination of the effective viscosity of non-Newtonian fluids flowing through porous media," Frontiers in Physics **7**, 71 (2019).